



NiO/Ni nanocomposites embedded in 3D porous carbon with high performance for lithium-ion storage

Zefang Yang¹ , Zhicheng Li¹ , Pengfei Li¹ , Caiyun Gao¹ , and Hong Zhang^{1,*}

¹School of Materials Science and Engineering, Central South University, Changsha 410083, China

Received: 25 June 2019

Accepted: 22 September 2019

Published online:

1 October 2019

© Springer Science+Business Media, LLC, part of Springer Nature 2019

ABSTRACT

The high energy storage devices such as lithium-ion batteries (LIBs) have recently attracted extensive attention, and massive efforts have been made to synthesize the high-performance electrodes for Li-ion storage. Here, a facile in situ synthesis method was proposed to prepare the NiO/Ni nanocomposites embedded in three-dimensional (3D) porous carbon network (denoted as NiO/Ni⊕C). The phase component and microstructure of the NiO/Ni⊕C were detected by using X-ray diffraction, scanning electron microscope and transmission electron microscopy. The NiO/Ni nanocomposites with the particle size of approximately 20–50 nm were uniformly dispersed in the 3D porous carbon matrix. The 3D carbon network is in favor of electrical conductivity, and effectively alleviates the volume effect during lithiation–delithiation processes, and thus help the electrode achieve high electrochemistry performance. The NiO/Ni⊕C electrodes possess a reversible specific capacity of 934 mAh g⁻¹ at a current density of 300 mA g⁻¹, and exhibit a superior rate performance with a specific capacity of 505 mAh g⁻¹ at a current density of 2 A g⁻¹. The NiO/Ni⊕C electrodes maintained a specific capacity of up to 683 mAh g⁻¹ even after 1000 cycles at a current density of 1 A g⁻¹.

Introduction

With the increasing energy demand from the emerging technologies such as portable electronics and electric vehicles (EVs), the high-efficiency energy storage devices such as supercapacitors, lithium-ion batteries (LIBs) and solar cells have attracted extensive attention [1–3], where LIBs are highly desirable owing to their high power and energy densities, low cost and long life [4–7]. However, the commercial

graphite anode exhibits a relatively low theoretical specific capacity of 372 mAh g⁻¹ and is not able to meet the requirements of emerging applications such as EVs [8, 9]. The transition metal oxides (TMOs) such as MnO, CoO, NiO, Fe₃O₄ and CuO possess remarkably higher theoretical specific capacities (> 600 mAh g⁻¹) than those of the current commercial anode materials of graphite and Li₄Ti₅O₁₂, and have been extensively studied as anode materials for high-performance LIBs in recent years [10–13]. In

Address correspondence to E-mail: hzhang@csu.edu.cn

particular, NiO has been widely studied for the applications in LIBs anode due to its high theoretical specific capacity (718 mAh g^{-1}), low cost, low toxicity and abundant resources [13–18]. Unfortunately, the electrochemical performance of NiO anodes is limited by its poor electrical conductivity and large volume variation during the lithiation–delithiation processes.

To address the above issues, many strategies including nanoparticles, hollow sphere structures, carbon-coated or carbonaceous materials and element doping have been developed [19–23]. Nano-sized materials can reduce the diffusion pathway of ions and electrons, and promote close contact between the electrode and electrolyte to enhance electrochemical performance [21, 22]. However, nanoscale materials can be easily aggregated and pulverized during electrochemical cycle processes, resulting in poor cycle stability [17]. The hollow structure has a large contact area between the electrode and the electrolyte, and also accommodates the mechanical strain caused by continuous Li^+ ions insertion/extraction [24, 25]. However, it is difficult to control the microscopic appearance of the hollow structure, and the synthesis method is complicated. Therefore, a series of TMOs/carbon hybrids attracted much attention [26–31]. For instance, Wang and co-workers synthesized 3D hierarchical porous NiO@carbon nanoflakes on graphene sheets through a solvothermal process and showed a capacity of 754 mAh g^{-1} after 50 cycles [26]. Fang et al. [27] reported that sandwich-structured graphene-metal oxide composites (NiO) prepared by thermal decomposition can deliver a capacity of 460 mAh g^{-1} for up to 100 cycles. Oh et al. [28] prepared mesoporous multicomponent metal oxide microspheres containing Ni and Mo components and N-doped carbon, in which 3D-ordered 40-nm-sized mesopores are interconnected, through spray pyrolysis. After 1000 cycles, the microspheres deliver a discharge capacity of 693 mAh g^{-1} at a current density of 1.0 A g^{-1} . The discharge capacity of the peapod NiO nanoparticles encapsulated in carbon fiber stabilized at 1193 mAh g^{-1} after 200 cycles at 500 mA g^{-1} [29], and the discharge capacity was 951 mAh g^{-1} for yolk–shell NiO powders after 150 cycles at 700 mA g^{-1} [30].

In this work, we developed a facile in situ synthesis strategy for the construction of NiO/Ni nanocomposites embedded in 3D porous carbon networks

(denoted as NiO/Ni⊕C). The prepared NiO/Ni⊕C exhibited high specific capacity and durable cycling life (683 mAh g^{-1} after 1000 cycles at the current density of 1000 mA g^{-1}) as lithium storage electrodes in LIBs.

Experimental

Synthesis process

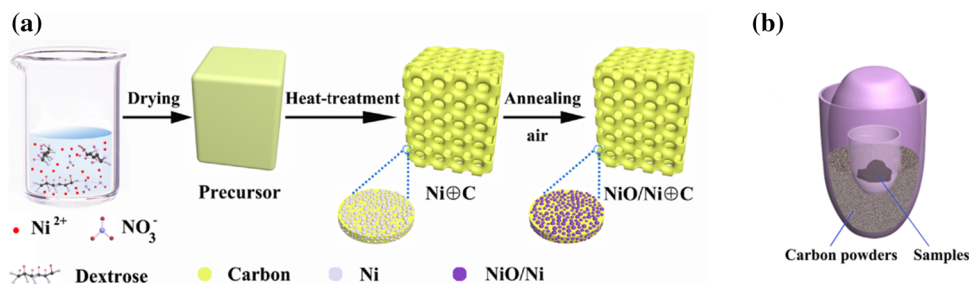
The typical fabrication process of the NiO/Ni nanocomposite embedded in 3D porous carbon networks is schematically illustrated in Fig. 1. 0.6 mmol nickel carbonate ($\text{NiCO}_3 \cdot 2\text{Ni}(\text{OH})_2 \cdot 4\text{H}_2\text{O}$, $\geq 99.0\%$, Xilong Scientific, China) and 0.01 mol glucose ($\text{C}_6\text{H}_{12}\text{O}_6 \cdot \text{H}_2\text{O}$, $\geq 99.0\%$, Hengxing, China) were completely dissolved into 10 mL diluted nitric acid. The solution was dried in an electron oven at $80 \text{ }^\circ\text{C}$ for 24 h to obtain precursor. Then the precursor was heat-treated at $700 \text{ }^\circ\text{C}$ for 2 h in the muffle furnace inside the laboratory-made setup (LMS, see in Fig. 1b). Inside the LMS, the reducing atmosphere with carbon monoxide was formed by the insufficient oxidation of carbon powders at high temperature for limited oxygen. So the nickel-based compounds such as NiO or $\text{Ni}(\text{OH})_2$ were reduced and Ni nanoparticles occurred, while the glucose was in situ carbonized to coat the Ni nanoparticles. As a result, Ni nanoparticles embedded in 3D carbon matrix (Ni⊕C) were received. More importantly, the 3D porous network materials with lots of voids formed spontaneously due to the escaping gases during the heat treatment. Finally, the black color Ni⊕C was annealed at different temperatures and holding periods ($250 \text{ }^\circ\text{C}$ for 2 h , $270 \text{ }^\circ\text{C}$ for 2 h , $270 \text{ }^\circ\text{C}$ for 4 h and $300 \text{ }^\circ\text{C}$ for 2 h) in air atmosphere in order to partially oxidize the nanostructured Ni and to fabricate the NiO/Ni nanocomposites embedded in 3D carbon network (NiO/Ni⊕C).

For comparison, carbon-free NiO nanoparticles were also synthesized directly for the investigations by heat treatment of precursors at $700 \text{ }^\circ\text{C}$ for 2 h in air without LMS container.

Materials characterization

The crystal structure of as-prepared products were detected through X-ray diffraction (XRD, Rigaku D/max 2550, Japan) with Cu K_α radiation and

Figure 1 Schematic illustration of the synthesis of NiO/Ni nanocomposites embedded in 3D carbon network (NiO/Ni⊕C), **a** fabrication procedure and **b** laboratory-made setup (LMS).



$\lambda = 0.154056$ nm, in the diffraction angles 2θ ranging from 10° to 80° . The morphology of samples was collected by using a field-emission scanning electron microscopy (SEM, FEI Nova NanoSEM230 and JSM 7900F). Elemental mapping was performed with an energy-dispersive X-ray spectroscopy (EDS, Oxford) appended to the SEM. Microstructures and crystalline phase were analyzed by using a high-resolution transmission electron microscopy (HRTEM, Tecnai G² F20, FEI). Thermogravimetric analysis (TGA) (NETZSCH STA 449c) was carried out in air from room temperature to 800°C with a heating rate of $10^\circ\text{C min}^{-1}$. Raman spectrum was recorded at ambient temperature with HORIBA LabRAM HR800 Raman spectrometer.

Cell assembly and electrochemical measurement

The working electrodes were made through the preparation of slurry followed by coating of electrode films. To prepare the electrode slurry, active materials such as NiO/Ni⊕C nanocomposites or carbon-free NiO nanoparticles, conductivity agent of carbon black and binder (polyvinylidene fluoride, PVDF) in the weight ratios of 8:1:1 were mixed with N-methyl pyrrolidone (NMP) as solvent. The electrode films were prepared by coating the slurry onto copper foils, and then were vacuum-dried at 60°C for 12 h. The coin-type 2016 cells, in which lithium metal acts as reference/counter electrode, and the prepared electrode film acting as working electrode were assembled in a glove box filled with ultra-high-purity argon. Polypropylene membrane (Celgard 3501) was used as separators in the cells. The electrolyte consists of a solution of 1 M LiPF₆ in ethylene carbonate (EC) and dimethyl carbonate (DEC) mixture (the volume ratio of EC to DEC is 1:1). The mass loading of active materials is about $0.9\text{--}1.1$ mg cm⁻².

The electrochemical measurements were carried out using a Land CT2001 test system within $0.01\text{--}3$ V at different current densities. Cyclic voltammetry (CV) tests were performed with an electrochemical workstation (Gamry Reference 600, USA) at a scan rate of 0.1 mV s⁻¹. The alternating current (AC) impedance measurements were performed in the Gamry electrochemical workstation in frequency range of 0.1 Hz to 1 MHz.

Results and discussion

XRD phase characterization

The phase components of the heat-treated samples and annealed samples were characterized by XRD patterns. The XRD pattern of the sample in which the precursor was only heat-treated at 700°C inside LMS is shown in Fig. 2a (marked by “before anneal”). Clear XRD peaks corresponding to the metallic Ni (refereed by JCPDS no. 87-0712) can be detected. According to the Scherrer formula, the average grain size of the metallic Ni was calculated to be about 10 nm. These indicate that the Ni⊕C powder was obtained after the precursor has been heat-treated at 700°C for 2 h in LMS, while, obtained from XRD pattern in Fig. 2b, the sample in which the precursor had been heat-treated at 700°C without LMS is only composed of NiO crystal phase (denoted as carbon-free NiO). Calculated by the Scherrer formula, the carbon-free NiO has the average grain size of about 53 nm.

The XRD patterns of the samples annealed at 250°C for 2 h, 270°C for 2 h, 270°C for 4 h and 300°C for 2 h are shown in Fig. 2a. It can be seen that all samples contain two series of XRD peaks corresponding to NiO phase with space group of $Fm\bar{3}m$ (JCPDS no. 75-0197) and metallic Ni, except for the sample annealed at 300°C for 2 h. In addition,

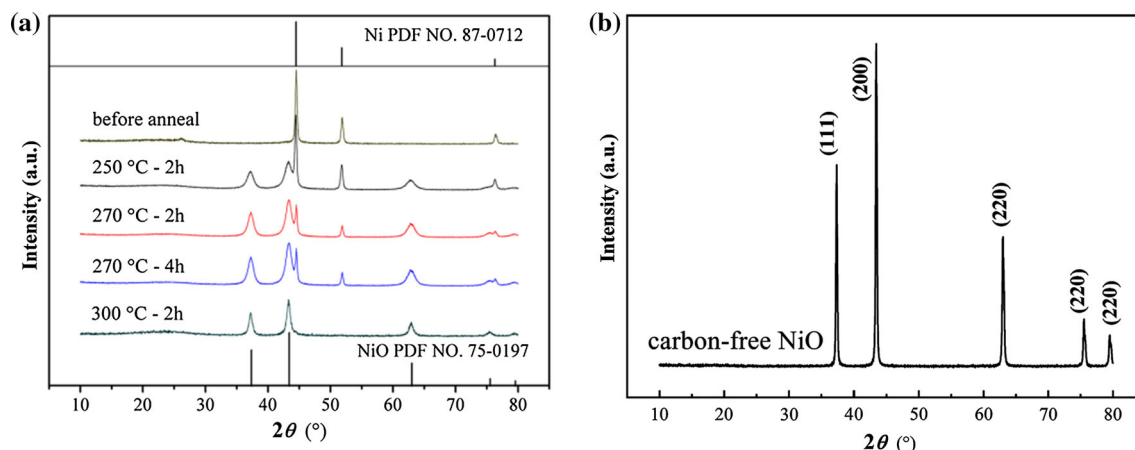


Figure 2 XRD patterns of the as-prepared products at various conditions, **a** 700 °C heat-treated in LMS (noted by “before anneal”), and further annealed at various temperatures/times in air,

only partial Ni was oxidized to NiO when the sample was annealed at 250 °C for 2 h, compared to the one annealed at 270 °C for 2 h. However, increasing the holding time at 270 °C has little effect on the strength of XRD peaks of NiO, comparing with the ones annealed for 2 h and 4 h. Refining the diffraction peaks at 2θ in the range of 32–80° with the Jade 6.0 program, the quasi-quantitative analysis showed that the content ratios of NiO to Ni are 0:1 (before annealing), 2.24:1 (250 °C for 2 h), 7:1 (270 °C for 2 h), 7.13:1 (270 °C for 4 h) and 1:0 (300 °C for 2 h), respectively. Based on the results, the sample annealed at 270 °C for 2 h was selected for the detailed investigation in this work. Analyzed by using the Scherrer formula, the average grain sizes were calculated to be 32 nm and 11 nm for Ni and NiO phases, respectively, in the sample annealed at 270 °C for 2 h. Therefore, one can get that the NiO/Ni⊕C nanocomposites were successfully obtained after the sample had been annealed at 270 °C for 2 h in air.

Microstructure characterization

Figure 3a–c shows the SEM observations of sample obtained from the precursor after being heat-treated in LMS at 700 °C. Figure 3a, b indicates that the sample consists of continuous network structure with 3D porous characteristics. It can be clearly seen from the enlarged view in Fig. 3c that white-colored nanostructured particles dispersed and embedded in the 3D gray color matrix which contains lots of nanostructured pores. To clarify the elemental

where the XRD patterns of metallic Ni and NiO were also provided for comparisons and **b** 700 °C heat-treated in air without LMS.

distribution in the sample, elemental mapping analysis was performed by SEM–EDS and the corresponding results are shown in Fig. 3d–f. Combined with the XRD in Fig. 2a, one can get that the white-colored nanostructured particles, as shown in Fig. 3c, d should be metallic Ni and the gray color matrix is composed of C element, and Ni nanoparticles are uniformly distributed in the 3D porous carbon network. These indicate that the samples with Ni nanoparticles embedded in 3D carbon matrix (Ni⊕C) have been successfully obtained after the precursor had been heat-treated at 700 °C for 2 h in LMS in this work.

After the Ni⊕C nanocomposites have been annealed at 270 °C for 2 h in air, the products as shown in Fig. 4a, b consist of more macropores when it is compared to the ones in Fig. 3a, b. The products, as shown in Fig. 4c, maintain favorable 3D porous networks with the NiO/Ni nanocomposites uniformly dispersed in the carbon matrix, as shown in Fig. 3. SEM–EDS elemental mappings in the NiO/Ni⊕C sample were induced and are shown in Fig. 4d–g. One can see that the Ni and O elements display almost the same distribution characteristic between Fig. 4d, e indicating that the oxidation of Ni had taken place during the annealing. Combined with the XRD analysis in Fig. 2, one can believe that the NiO/Ni nanocomposites uniformly dispersed in the porous carbon frameworks, i.e., NiO/Ni⊕C nanocomposites, were successfully fabricated.

Transmission electron microscopy (TEM) is a powerful tool to disclose more detailed structure in

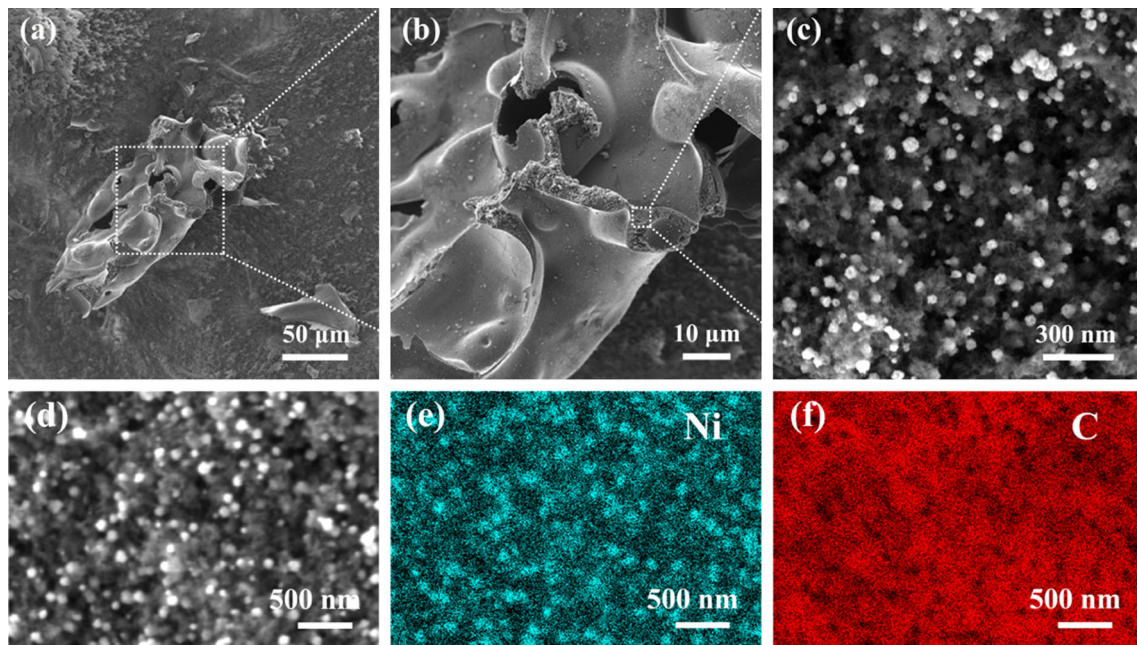


Figure 3 SEM investigations of product heat-treated at 700 °C in LMS, **a, b** secondary electron images, **c** back-scattered electron image recorded from the section in **b**; **d, e, f** SEM image and related EDS elemental mappings of Ni and C.

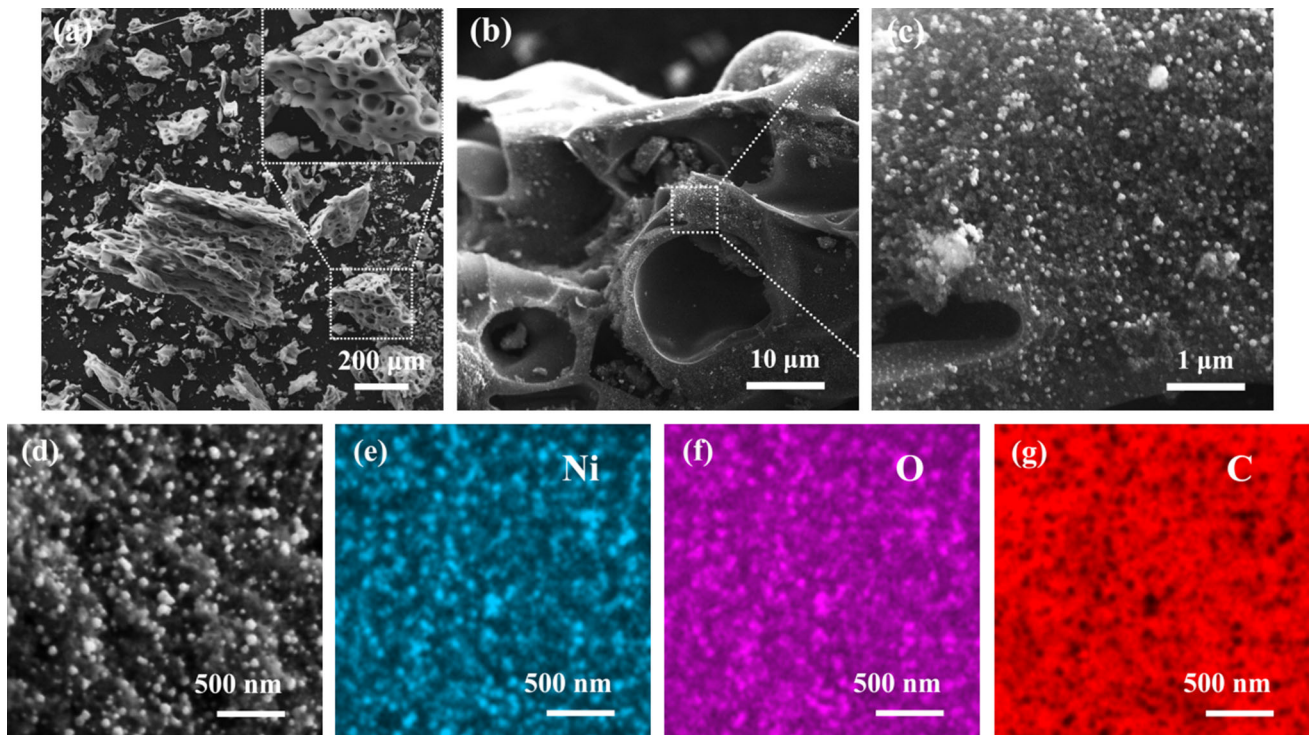


Figure 4 SEM investigations of product heat-treated at 700 °C in LMS followed by 270 °C annealing in air for 2 h, **a, b** secondary electron images, **c** back-scattered electron image recorded from the

marked area in **b**; **d, e, f, g** SEM image and corresponding EDS elemental mappings of the Ni, O and C elements, respectively.

nano- and even atomic scales. Figure 5a, b shows the TEM images of the NiO/Ni⊕C nanocomposites that were made from the intermediate product Ni⊕C after being 270 °C annealing. One can see that a large number of NiO/Ni nanocomposites with size of about 20–50 nm are uniformly distributed in the amorphous carbon layer. Figure 5c provides a high-resolution TEM (HRTEM) image and an upper-right inset SAED pattern of the crystalline structure of the NiO/Ni⊕C nanocomposite. The (111), (200) and (220) planes of NiO, and (200) and (220) planes of Ni can be indexed from the SAED pattern. In the meanwhile, the lattice spacings of about 0.243 and 0.203 nm corresponding to the (111) of NiO and Ni, respectively, can be detected in the HRTEM image. This further reveals the fact of NiO/Ni⊕C nanocomposite structure.

For comparison, it is shown in the TEM analysis in Fig. 5d–f of the carbon-free NiO products that the precursors were heat-treated at 700 °C for 2 h in air without LMS. The particle sizes are between 100 and 200 nm, which is obviously larger than that of NiO/Ni⊕C nanocomposites. The HRTEM image and an upper-right inset SAED pattern in Fig. 4f reveal that

the product is only composed of NiO crystals, and no metallic Ni and carbon could be found.

In order to confirm the existence and structure of carbon in the NiO/Ni⊕C nanocomposites, Raman spectroscopy (RS) analysis was performed as shown in Fig. 6a. It is clear that a broaden peak at 1317 cm^{-1} (D-band) represents a highly disordered graphite arrangement and another peak at 1585 cm^{-1} (G-band) represents an ordered graphite structure [32]. The D-band is caused by the vibration of the carbon atoms that terminate in the plane of the disordered graphite component. The G-band corresponds to the E_{2g} mode caused by the stretching vibrations of the sp^2 -bonded carbon atoms in the two-dimensional hexagonal lattice. The intensity ratio of D- and G-bands (I_D/I_G) of 1.1 further indicates the relative disorder level of carbon. The total weight change in the NiO/Ni⊕C nanocomposite was determined by the thermogravimetric analysis (TGA) as shown in Fig. 6b. A weight loss taking place below 100 °C should be attributed to volatilization of absorbed water. On the other hand, the weight loss of 41.4% in the temperature range of 200–620 °C should result from the oxidation of carbon (the weight denoted as

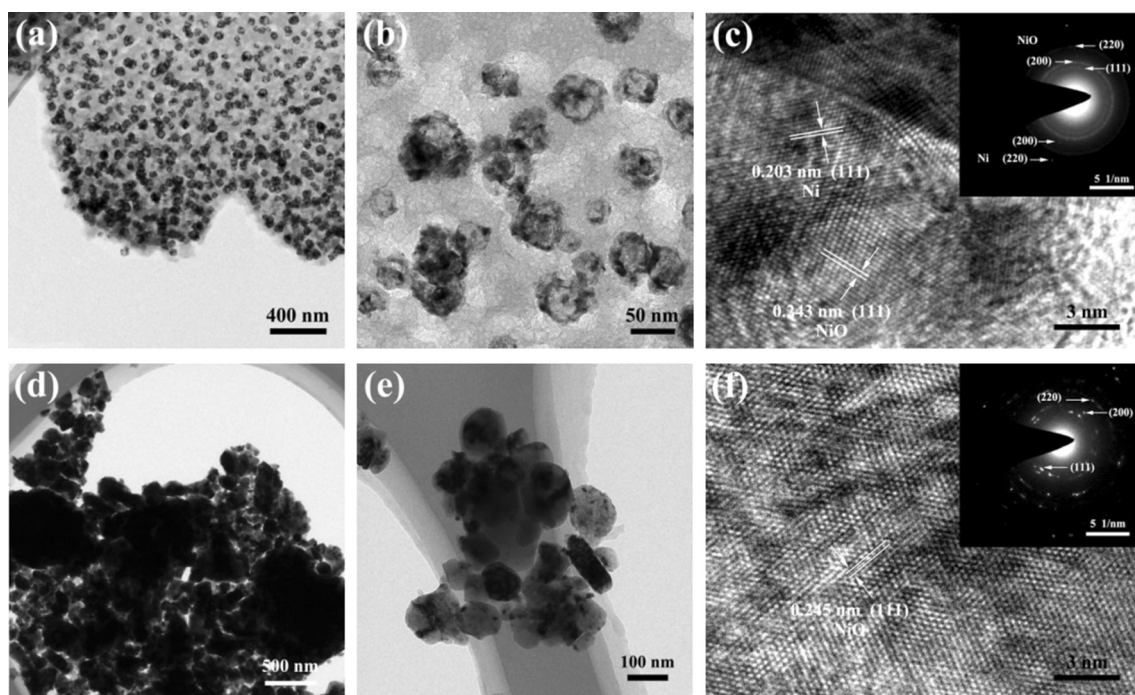


Figure 5 TEM investigations, a, b bright-field TEM images of a sample made from the intermediate product Ni⊕C after being annealed at 270 °C, c HRTEM image and upper-right inset SAED pattern recorded from the same sample as that in a. d, e bright-

field TEM images of a sample made from the precursor after being heat-treated at 700 °C without LMS, f HRTEM image and upper-right inset SAED pattern recorded from the sample as that in d.

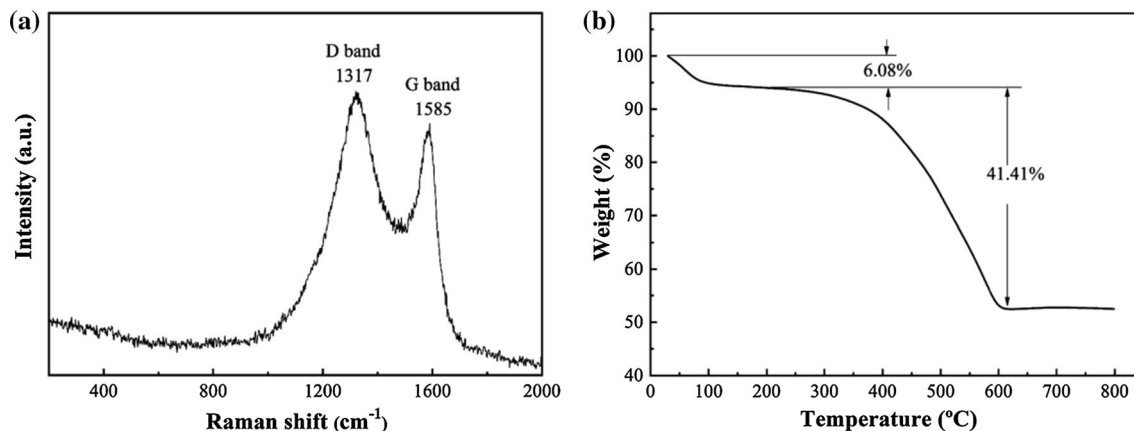


Figure 6 a Raman spectrum and b TGA profile of the sample NiO/Ni⊕C nanocomposite.

m_C , same as follows) to CO_2 or CO and related volatilization, as well as the weight gain ($m_{\text{Ni}\uparrow}$) caused by the oxidation of residual Ni (m_{Ni}), i.e.,

$$m_C - m_{\text{Ni}\uparrow} = 41.4\% \quad (1)$$

The weight increase rate of Ni oxidation to NiO is about 27% according to the related molar weights. On the other hand, from the results of XRD analysis, the content ratios of NiO (m_{NiO}) to Ni are 7:1 after being annealed at 270 °C for 2 h. And the total content of m_{Ni} , m_{NiO} and m_C is 100%. So, one can get that the net amount of residual Ni (m_{Ni}) was calculated to be about 6.5%. This also indicates that the remaining nickel is about 1.75% after being annealed at 270 °C for 2 h. Finally, the content of carbon in the NiO/Ni⊕C nanocomposite was calculated as 39.65%.

Electrochemical performance

Figure 7a shows the cyclic voltammetric (CV) curves of a cell assembled by the NiO/Ni⊕C electrode, tested between 0.01 and 3.0 V at a scan rate of 0.1 mV s^{-1} . In the first cycle, the reduction peak locating at 0.52 V (vs. Li/Li⁺) corresponds to the conversion process from NiO to Ni and the formation of solid electrolyte interface (SEI) layer [33, 34]. In addition, a smaller oxidation peak at 1.46 V and a relatively strong oxidation peak at 2.24 V can be seen, which should result from the delithiation reactions of Ni and Li_2O as proposed by Ma et al. [35]. The related electrochemical reactions can be described as $0.5\text{Ni} + \text{Li}_2\text{O} - \text{e}^- \rightarrow \text{Li}^+ + 0.5\text{Li}_2\text{NiO}_2$ (around 1.46 V) and $\text{Li}^+ + 0.5\text{Li}_2\text{NiO}_2 - \text{e}^- \rightarrow \text{Li}^+ + \text{NiO}$ (around 2.24 V). In the following cycles, the reduction peaks shifted to about 1.4 V (for NiO \rightarrow Li_2NiO_2) and about

1.02 V (for $\text{Li}_2\text{NiO}_2 \rightarrow \text{Ni}$), while the oxidation peaks did not change obviously. Meanwhile, the CV profiles maintained good repeatability since the second cycle, indicating that a stable SEI film formed on the surfaces of carbon layers in the first cycle and the electrode kept repeatable lithiation–delithiation processes. The galvanostatic charge–discharge curves of NiO/Ni⊕C and carbon-free NiO electrodes in the voltage range of 0.01–3.0 V versus Li/Li⁺ under a current density of 300 mA g^{-1} are presented in Fig. 7b, respectively. As shown in the inset in Fig. 7b, the NiO/Ni⊕C electrode exhibits a higher potential plateau (~ 0.68 V) than that of the carbon-free NiO electrode (0.51 V) in the first discharge process. It can be found that the NiO/Ni⊕C electrode reached a discharge specific capacity of 1943 mAh g^{-1} in the first cycle, but a charge specific capacity of 1059 mAh g^{-1} was achieved in the second cycle. The irreversible capacity loss may be attributed to the formation of SEI layer [5, 14, 36, 37], and from the irreversible capacitance for the effect of quasi-capacitor for the high specific surface of the NiO/Ni⊕C electrode. It is worth noting that the specific capacities became gradually stable in the subsequent cycles, and remained 934 mAh g^{-1} even after 200 cycles. These capacities are much higher than the theoretical capacity of NiO (718 mAh g^{-1}). However, the specific capacity of the carbon-free NiO electrode was only 123 mAh g^{-1} in the tenth cycle (see in Fig. 7c). The excellent stability of the NiO/Ni⊕C electrode should be attributed to the 3D porous network structure of NiO/Ni⊕C nanocomposites and the existence of carbon layer, which effectively protect the active materials from agglomeration and pulverization.

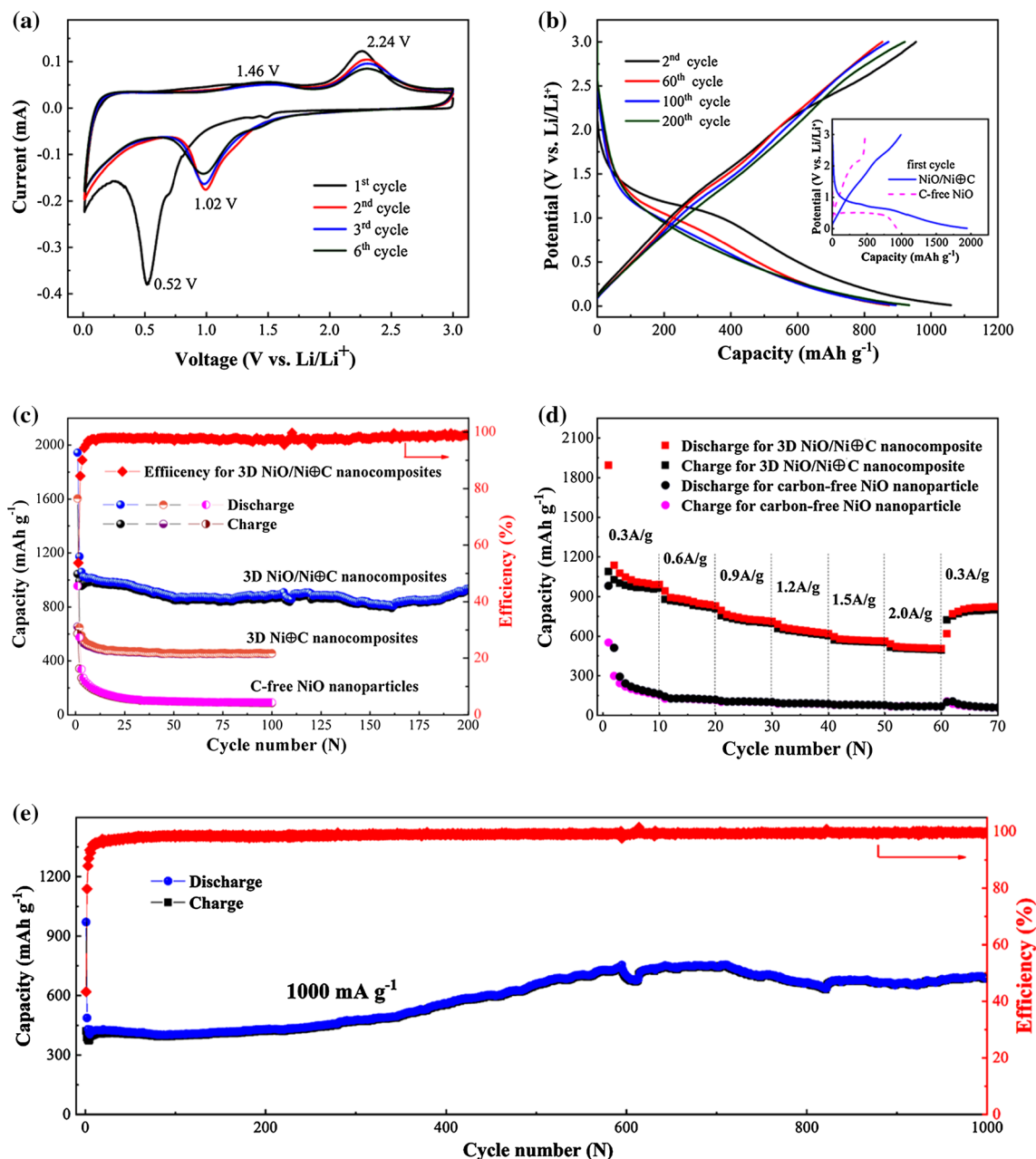


Figure 7 Electrochemical performance of the studied electrodes, **a** CV curves of NiO/Ni@C electrode at scan rate of 0.1 mV s^{-1} , **b** charge/discharge curves of NiO/Ni@C electrodes at a current density of 300 mA g^{-1} , inset shows comparison of first charge/discharge curves of NiO/Ni@C and carbon-free NiO electrodes,

c comparison of cycling performance of NiO/Ni@C, Ni@C and carbon-free NiO electrodes at 300 mA g^{-1} , **d** comparison of rate performance of NiO/Ni@C and carbon-free NiO electrodes at various current densities, **e** cycling performance of NiO/Ni@C electrode at a current density of 1000 mA g^{-1} for 1000 cycles.

Cycling performance is a key aspect for evaluating the electrode materials for LIBs. Figure 7c depicts the comparison of cycling performance of NiO/Ni@C, Ni@C and carbon-free NiO electrodes at a constant current density of 300 mA g^{-1} . Obviously, the NiO/Ni@C electrode exhibited a much better cycle retention and much higher reversible capacities than the

carbon-free NiO electrode. The NiO/Ni@C electrode contained a high reversible capacity of 934 mAh g^{-1} after 200 cycles. Moreover, the Coulombic efficiency rapidly increased from 54% for the first cycle to about 98% after the fifth cycle and closes to 100% thereafter, suggesting an agile lithium insertion/extraction associated with efficient transport of ions and

Table 1 Comparison of electrochemical properties of 3D porous NiO/Ni⊕C nanocomposite with the previously reported NiO-based anode materials

Materials	Current density (mA g ⁻¹)	Cycle number	Capacity retention (mAh g ⁻¹)	References
3D porous NiO/Ni⊕C	300	200	934	This work
3D porous NiO/Ni⊕C	1000	1000	683	This work
NiO nanocrystals	100	50	900	[13]
NiO–graphene composites	100	200	594.8	[17]
NiO/C hollow microspheres	100	100	628	[24]
Hollow NiO microspheres	100	50	640	[38]
Hierarchical 1D NiO	1000	40	823	[39]
NiO nanobelt	2000	515	416	[40]
NiO hybrid nanospheres	100	100	863	[41]
Egg yolk–shell NiO/C	100	100	625.3	[42]

electrons in the NiO/Ni⊕C electrodes. Furthermore, the Ni⊕C electrode shows a stable specific capacity of 454 mAh g⁻¹ after 100 cycles. However, the capacities of carbon-free NiO nanoparticles faded quickly during the first few cycles. At the end of 40 cycles, only 104 mAh g⁻¹ was delivered by the carbon-free NiO electrode. These demonstrate the obviously positive effect of the unique 3D porous carbon network in which the NiO/Ni nanocomposites were embedded. On the other hand, the characteristic of the elastic carbon layers can accommodate the volume expansion of active materials during lithiation/delithiation processes and keep the electrode from being broken. Furthermore, the porous carbon wrapping NiO/Ni nanocomposites can effectively enhance the electronic conductivity inside the electrode. Therefore, the 3D NiO/Ni⊕C electrodes exhibit obviously excellent electrochemical performance compared to the carbon-free NiO nanoparticles.

In order to better understand the superiority of NiO/Ni⊕C electrode, galvanostatic charge/discharge tests at different current densities are carried out. As shown in Fig. 7d, as the current densities increased from 0.3 A g⁻¹ to 0.6, 0.9, 1.2, 1.5, and 2 A g⁻¹ for the NiO/Ni⊕C electrode, the specific discharge capacities changed from 989 mAh g⁻¹ to 827, 711, 619, 561 and 505 mAh g⁻¹, respectively. Even at the high rate of 2 A g⁻¹, the reversible capacity remains at about 505 mAh g⁻¹, which is still higher than the theoretical specific capacity of graphite electrode (ca. 372 mAh g⁻¹). In addition, when the current density was switched to 0.3 A g⁻¹, the NiO/Ni⊕C electrode still maintained a capacity of 821 mAh g⁻¹. However, the carbon-free NiO

electrode exhibited the capacities of 161, 118, 101, 87, 77 and 66.7 mAh g⁻¹ under the corresponding current densities, respectively, as that induced in the NiO/Ni⊕C electrode. Compared with the NiO/Ni⊕C electrodes, the carbon-free NiO electrode has obviously weak electrochemical performance. To gain further insight into the cycle stability of the NiO/Ni⊕C electrode, the charge/discharge performance was performed at a high current density of 1 A g⁻¹. As shown in Fig. 7e, the reversible discharge capacities of about 470 mAh g⁻¹ were received in the first 300 cycles, and then an increased discharge capacity was observed as 692 mAh g⁻¹ at the 600th cycle, and the capacity of 683 mAh g⁻¹ at the 1000th cycle was kept. Apparently, the NiO/Ni⊕C electrode exhibited obvious superiority in electrochemical performance compared with the reported NiO-based anode materials (see in Table 1).

The assembled half-cells were subjected to an alternating current (AC) impedance test, after being electrochemically cycled at 1 A g⁻¹ for 10, 300, 600 and 1000 cycles, respectively. Figure 8a depicts the Nyquist plots of the NiO/Ni⊕C electrode at different electrochemical statuses. The corresponding equivalent circuit is established as shown in the inset, where R_s reflects the solution resistance, and CPE_f and CPE_{ct} represent the constant phase elements for the capacitance effect of the SEI film resistance and the charge-transfer resistance.

For the impedance spectrum of the fresh cell, only one arc was observed at high frequency, suggesting that the SEI layer has not yet formed [43]. The other curves consist of an arc in the high-frequency region and one in the medium-frequency region and a

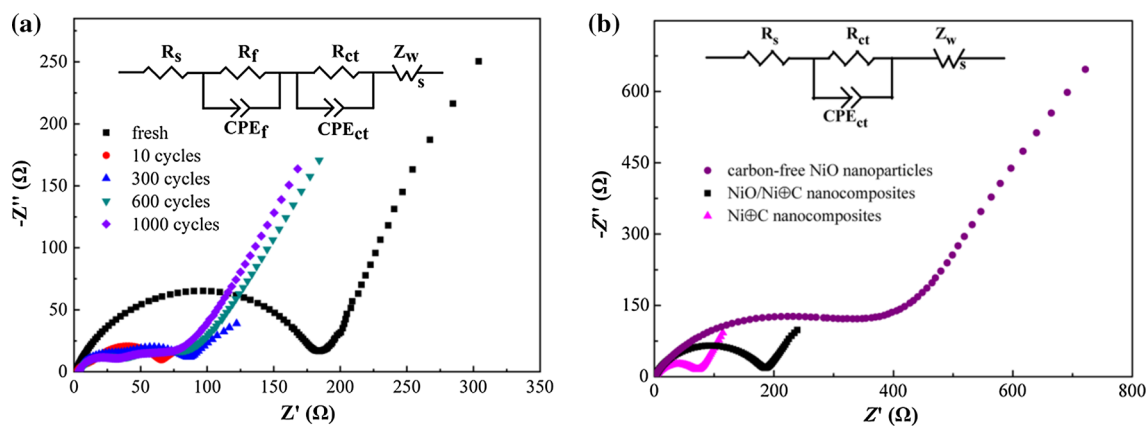


Figure 8 Nyquist plots of complex impedance spectra at different electrochemical statuses, and the inset equivalent circuit for spectrum fitting, **a** fresh cell, after being cycled 10, 300, 600

and 1000 cycles for NiO/Ni⊕C electrode, **b** fresh cells assembled with NiO/Ni⊕C, Ni⊕C and carbon-free NiO electrodes.

Table 2 Fitted data of impedance spectra shown in Fig. 8 for NiO/Ni⊕C, Ni⊕C and C-free NiO electrodes

Samples	R_s (Ω)	R_f (Ω)	R_{ct} (Ω)
C-free NiO fresh	1.37		339.80
NiO/Ni⊕C fresh	1.49		180.60
Ni⊕C fresh	1.84		69.62
NiO/Ni⊕C 10 cycles	2.38	8.61	55.40
NiO/Ni⊕C 300 cycles	3.44	24.00	54.00
NiO/Ni⊕C 600 cycles	3.61	24.00	51.60
NiO/Ni⊕C 1000 cycles	4.68	26.03	58.28

sloping line in the low-frequency region. The two arcs should correspond to the SEI film resistance (R_f) and charge-transfer resistance (R_{ct}), while the sloping line is related to Warburg resistance (Z_w) that reflects the Li^+ ions diffusion in the electrode. The impedance values fitted by equivalent circuit are collected in Table 2. It can be seen that R_{ct} was 180.6 Ω before electrochemical tests, and decreased to 55.4 Ω after ten cycles, suggesting that the activation process took place in the electrode during the initial cycles [35, 44]. The small change in R_{ct} from 10 to 1000 cycles indicates the high structural stability of the NiO/Ni⊕C nanocomposite during the lithiation/delithiation processes. In addition, the R_f delivered by the electrochemically inert layer (i.e., SEI film) formed on the surface of the active material in the initial cycles. The value of R_f did not show any significant change after the 300th cycle. The stability of SEI layer is mandatory for good rate capability and cycle stability, and is consistent with the high cycle life as shown in Fig. 7e.

To compare the electrical conductivity of the electrodes, Nyquist plots of both cells made from NiO/

Ni⊕C nanocomposites, Ni⊕C nanocomposites and carbon-free NiO nanoparticles electrodes before cycling are presented in Fig. 8b. It is observed that the R_{ct} of Ni⊕C nanocomposite electrode is much lower than that of the carbon-free NiO nanoparticle and NiO/Ni⊕C nanocomposite electrode, demonstrating better charge-transfer kinetics in the Ni⊕C electrode. This can prove that the metal Ni and carbon in the NiO/Ni⊕C nanocomposite simultaneously contribute to high electrical conductivity. Besides, the lithium diffusion coefficient (D_{Li^+}) can be calculated from the low-frequency Warburg region using the following equations [45, 46].

$$Z' = R_s + R_{ct} + \sigma_\omega \omega^{-0.5} \quad (2)$$

$$D_{\text{Li}^+} = \frac{R^2 T^2}{2A^2 n^4 F^4 C^2 \sigma_\omega^2} \quad (3)$$

where R is the gas constant, T is the absolute temperature, A is the surface area of the electrode, n is the number of electrons per molecule during oxidation, F is the Faraday constant, C corresponds to the concentration of lithium ions and σ_ω is Warburg coefficient related to lithium-ion diffusion coefficient which can be obtained from Eq. [2]. The slope σ_ω can be obtained based on a linear fitting of Z' versus $\omega^{-1/2}$ as shown in Fig. 9. The estimated Warburg factor values of NiO/Ni⊕C and carbon-free NiO are 114.3, 918.8 $\Omega \text{ rad}^{-0.5} \text{ s}^{0.5}$, respectively. The corresponding Li^+ diffusion coefficient D_{Li^+} calculated from Eq. [3] is 4.64×10^{-15} and $7.65 \times 10^{-17} \text{ cm}^2 \text{ s}^{-1}$, respectively. This indicates that the NiO/Ni⊕C nanocomposite has a higher lithium diffusion coefficient and smaller charge-transfer resistance compared to

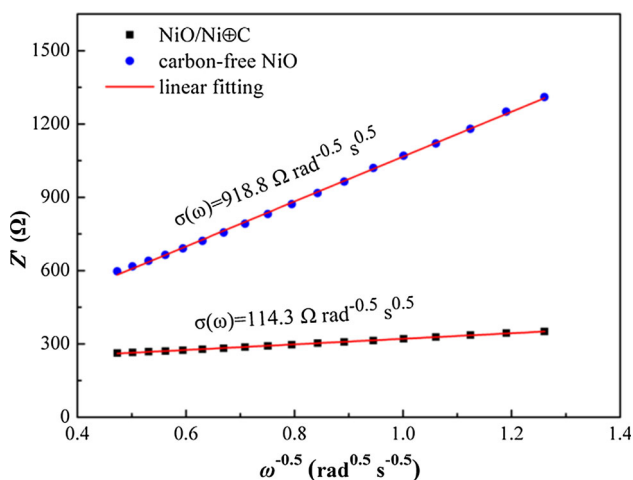
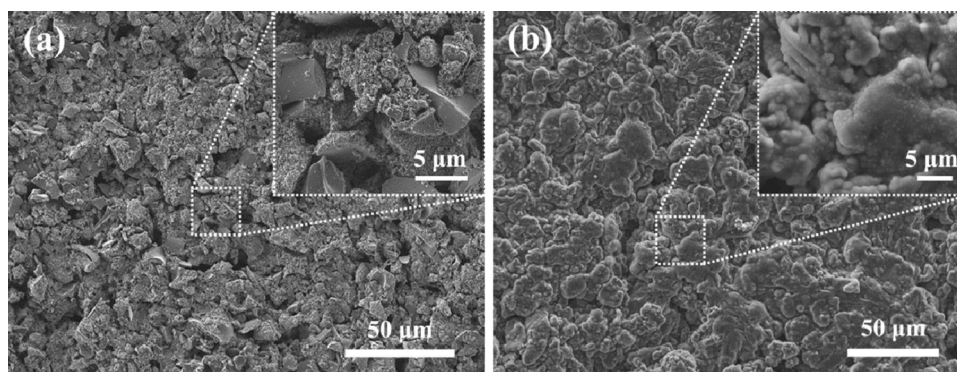


Figure 9 The relationship between Z' and $\omega^{-0.5}$ in the low-frequency region of NiO/Ni \oplus C and carbon-free NiO electrodes before the electrochemical cycle.

carbon-free NiO, which are favorable for enhancing the electrochemical performance. Furthermore, the unique 3D porous characteristic of the NiO/Ni \oplus C nanocomposite not only provides sufficient space to mitigate severe volume changes during the charge/discharge cycles, but also supplies abundant open channels and active sites for electrolyte penetration and Li⁺ ions residing, and thus promotes Li⁺ ions diffusion.

Figure 10 shows the SEM images of the NiO/Ni \oplus C electrode before and after 200 cycles at 300 mA g⁻¹. One can see that the NiO/Ni \oplus C nanocomposite was uniformly coated on the copper foil before the electrochemical cycle as shown in Fig. 10a. After 200 electrochemical cycles, as shown in Fig. 10b, the morphology characteristic of lump protuberances was observed; the electrode was still attached to the copper foil collector, and no pulverization of the electrode was found. These indicate that such 3D

Figure 10 SEM observations of NiO/Ni \oplus C electrode, **a** before cycle and **b** after 200 electrochemical cycles at 300 mA g⁻¹ (the residual electrolyte was removed by washing in anhydrous dimethyl carbonate).



porous connected network structure can indeed enhance the function of relieving the strain and stress caused by volume variation and preventing the agglomeration or detachment of inner NiO nanoparticles over cycling processes.

Based on the above discussion, the NiO/Ni \oplus C nanocomposite electrode exhibits an excellent electrochemical performance. The eminent properties should be attributed to its stable structure and is described in the following aspects. First, the porous carbon matrix, in which NiO/Ni nanocomposite is uniformly dispersed, constructs an efficient and continuous conductive network and effectively improves the electrode conductivity. Second, the amorphous carbon layer can protect the embedded NiO/Ni nanocomposite from directly contacting the electrolyte, thereby alleviating the side reaction between the active material and electrolyte. Finally, the elastic carbon networks can effectively inhibit the aggregation of NiO nanoparticles and mitigate volume expansion/contraction during the charge/discharge processes, and thus preserve the structural integrity of the whole electrode.

Conclusion

The NiO/Ni nanocomposites embedded in 3D porous carbon (NiO/Ni \oplus C) networks were successfully fabricated by 700 °C heat treatment in laboratory-made setup followed by annealing 270 °C in air of the precursors made from the mixture of nickel carbonate and glucose. The NiO/Ni \oplus C used as the Li-storage electrode for Li-ion batteries exhibits an excellent electrochemical property with a reversible specific capacity of 934 mAh g⁻¹ after 200 cycles at a current density of 300 mA g⁻¹. The NiO/Ni \oplus C electrode shows superior rate performance with a

specific capacity of 505 mAh g⁻¹ at a current density of 2 A g⁻¹ and has a capacity of up to 683 mAh g⁻¹ even after 1000 cycles at a high current density of 1 A g⁻¹. The present synthesis method is facile and effective, and is suitable for the scaled products.

Acknowledgements

This work is supported by the research funding from the Hunan Wedid Materials Technology Co., Ltd. (No. 738010241) and the National Natural Science Foundation of China (No. 51767021). Thanks are also due to Chen Qingshan, Xi Desheng, Cheng Huaqiu at JEOL for some SEM observations with JSM-7900F.

Compliance with ethical standards

Conflict of interest The authors declare that they have no conflict of interest.

References

- [1] Naoi K, Ishimoto S, Miyamoto JM, Naoi W (2012) Second generation nanohybrid supercapacitor evolution of capacitive energy storage devices. *Energy Environ Sci* 5:9363–9373
- [2] Liu C, Li F, Ma LP, Cheng HM (2010) Advanced materials for energy storage. *Adv Energy Mater* 22:E28–E62
- [3] Armand M, Tarascon JM (2008) Building better batteries. *Nature* 451:652–657
- [4] Dunn B, Kamath H, Tarascon JM (2011) Electrical energy storage for the grid: a battery of choices. *Science* 334:928–935
- [5] Liu S, Wang Z, Yu C, Wu HB, Wang G, Dong Q, Qiu J, Eychmüller A, Lou XW (2013) A flexible TiO₂(B)-based battery electrode with superior power rate and ultralong cycle life. *Adv Mater* 25:3462–3467
- [6] Yu Y, Yan C, Gu L, Lang X, Tang K, Zhang L, Hou Y, Wang Z, Chen MW, Schmidt OG, Maier J (2013) Three-dimensional (3D) bicontinuous Au/amorphous-Ge thin films as fast and high-capacity anodes for lithium-ion batteries. *Adv Energy Mater* 3:281–285
- [7] Yuan C, Wu HB, Xie Y, Lou XW (2014) Mixed transition-metal oxides: design, synthesis, and energy-related applications. *Angew Chem Int Edit* 53:1488–1504
- [8] Zhang J, Xie Z, Li W, Dong S, Qu M (2014) High-capacity graphene oxide/graphite/carbon nanotube composites for use in Li-ion battery anodes. *Carbon* 74:153–162
- [9] Cui Q, Zhong Y, Pan L, Zhang H, Yang Y, Liu D, Teng F, Bando Y, Yao J, Wang X (2018) Recent advances in designing high-capacity anode nanomaterials for Li-ion batteries and their atomic-scale storage mechanism studies. *Adv Sci* 5:1700902–1700923
- [10] Ko Y, Kwon M, Song Y, Lee SW, Cho J (2018) Thin-film electrode design for high volumetric electrochemical performance using metal sputtering combined ligand exchange layer-by-layer assembly. *Adv Funct Mater* 28:1804926–1804937
- [11] Zhu S, Li J, Deng X, He C, Liu E, He F, Shi C, Zhao N (2017) Ultrathin-nanosheet-induced synthesis of 3D transition metal oxides networks for lithium ion battery anodes. *Adv Funct Mater* 27:1605017–1605024
- [12] Wang B, Li F, Wang X, Wang G, Wang H, Bai J (2019) Mn₃O₄ nanotubes encapsulated by porous graphene sheets with enhanced electrochemical properties for lithium/sodium-ion batteries. *Chem Eng J* 364:57–69
- [13] Khalil A, Lalia BS, Hashaikeh R (2016) Nickel oxide nanocrystals as a lithium-ion battery anode: structure-performance relationship. *J Mater Sci* 51:6624–6638
- [14] Lee WW, Lee JM (2014) Novel synthesis of high performance anode materials for lithium-ion batteries (LIBs). *J Mater Chem A* 2:1589–1626
- [15] Poizot P, Laruelle S, Grugeon S, Dupont L, Tarascon JM (2000) Nano-sized transition-metal oxides as negative-electrode materials for lithium-ion batteries. *Nature* 407:496–499
- [16] Aricò AS, Bruce P, Scrosati B, Tarascon JM, Schalkwijk WV (2005) Nanostructured materials for advanced energy conversion and storage devices. *Nat Mater* 4:366–377
- [17] Chen J, Wang Z, Mu J, Ai B, Zhang T, Ge W, Zhang L (2018) Enhanced lithium storage capability enabled by metal nickel dotted NiO-graphene composites. *J Mater Sci* 54:1475–1487. <https://doi.org/10.1007/s10853-018-2882-3>
- [18] Liang J, Hu H, Park H, Xiao C, Ding S, Paik U, Lou XW (2015) Construction of hybrid bowl-like structures by anchoring nio nanosheets on flat carbon hollow particles with enhanced lithium storage properties. *Energy Environ Sci* 8:1707–1711
- [19] Zhang J, Yu A (2015) Nanostructured transition metal oxides as advanced anodes for lithium-ion batteries. *Sci Bull* 60:823–838
- [20] Zhan Y, Liu N (2017) Nanostructured electrode materials for high-energy rechargeable Li. Na and Zn batteries, *Chem Mater* 29:9589–9604
- [21] Ai Q, Yuan Z, Huang R, Yang C, Jiang G, Xiong J, Huang Z, Yuan S (2018) One-pot co-precipitation synthesis of Fe₃O₄ nanoparticles embedded in 3d carbonaceous matrix as anode for lithium ion batteries. *J Mater Sci* 54:4212–4224. <https://doi.org/10.1007/s10853-018-3141-3>

- [22] Wang X, Feng J, Bai Y, Zhang Q, Yin Y (2016) Synthesis, properties, and applications of hollow micro-/nanostructures. *Chem Rev* 116:10983–11060
- [23] Tian J, Shao Q, Dong X, Zheng J, Pan D, Zhang X, Cao H, Hao L, Liu J, Mai X, Guo Z (2018) Bio-template synthesized NiO/C hollow microspheres with enhanced Li-ion battery electrochemical performance. *Electrochim Acta* 261:236–245
- [24] Yang Z, Su D, Yang J, Wang J (2017) Fe₃O₄/C composite with hollow spheres in porous 3D-nanostructure as anode material for the lithium-ion batteries. *J Power Sources* 363:161–167
- [25] Liu R, Shen C, Zhang C, Iocozzia J, Wang Q, Zhao S, Yuan K, Lin Z (2018) Hierarchical bicomponent TiO₂ hollow spheres as a new high-capacity anode material for lithium-ion batteries. *J Mater Sci* 53:8499–8509. <https://doi.org/10.1007/s10853-018-2195-6>
- [26] Wang X, Zhang L, Zhang Z, Yu A, Wu P (2016) Growth of 3D hierarchical porous NiO@carbon nanoflakes on graphene sheets for high-performance lithium-ion batteries. *Phys Chem Chem Phys* 18:3893–3899
- [27] Fang H, Zhao L, Yue W, Wang Y, Jiang Y, Zhang Y (2015) Facile and large-scale preparation of sandwich-structured graphene-metal oxide composites as anode materials for Li-ion batteries. *Electrochim Acta* 186:397–403
- [28] Oh SH, Kim JK, Kang YC, Cho JS (2018) Three-dimensionally ordered mesoporous multicomponent (Ni, Mo) metal oxide/N-doped carbon composite with superior Li-ion storage performance. *Nanoscale* 10:18734–18741
- [29] Feng Y, Zhang H, Zhang Y, Bai Y, Wang Y (2016) Novel peapod NiO nanoparticles encapsulated in carbon fibers for high-efficiency supercapacitors and lithium-ion batteries. *J Mater Chem A* 4:3267–3277
- [30] Choi SH, Kang YC (2014) Ultrafast synthesis of yolk-shell and cubic NiO nanopowders and application in lithium ion batteries. *ACS Appl Mater Int* 6:2312–2316
- [31] Ruan X, Yang Y, Pu K, Gao M, Liu Y, Pan H (2018) Superior long-term cyclability of a nanocrystalline NiO anode enabled by a mechanochemical reaction-induced amorphous protective layer for Li-ion batteries. *J Power Sources* 397:134–142
- [32] Pol VG, Thackeray MM (2011) Spherical carbon particles and carbon nanotubes prepared by autogenic reactions: evaluation as anodes in lithium electrochemical cells. *Energy Environ Sci* 4:1904–1912
- [33] Zou F, Chen YM, Liu K, Yu Z, Liang W, Bhaway SM, Gao M, Zhu Y (2016) Metal organic frameworks derived hierarchical hollow NiO/Ni/graphene composites for lithium and sodium storage. *ACS Nano* 10:377–386
- [34] Sun X, Yan C, Chen Y, Si W, Deng J, Oswald S, Liu L, Schmidt OG (2014) Three-dimensionally “curved” NiO nanomembranes as ultrahigh rate capability anodes for Li-ion batteries with long cycle lifetimes. *Adv Energy Mater* 4:1300912
- [35] Ma Z, Zhang H, Zhang Y, Zhang J, Li Z (2015) Electrochemical characteristics of nanostructured NiO plates hydrothermally treated on nickel foam for Li-ion storage. *Electrochim Acta* 176:1427–1433
- [36] Zhou X, Yin Y-X, Wan L-J, Guo Y-G (2012) Self-assembled nanocomposite of silicon nanoparticles encapsulated in graphene through electrostatic attraction for lithium-ion batteries. *Adv Energy Mater* 2:1086–1090
- [37] Chen D, Mei X, Ji G, Lu M, Xie J, Lu J, Lee JY (2012) Reversible lithium-ion storage in silver-treated nanoscale hollow porous silicon particles. *Angew Chem Int Edit* 51:2409–2413
- [38] Shao J, Zhou H, Feng J, Zhu M, Yuan A (2019) Facile synthesis of MOF-derived hollow NiO microspheres integrated with graphene foam for improved lithium-storage properties. *J Alloy Compds* 784:869–876
- [39] Zheng Q, Liu Y, Guo H, Hua X, Shi S, Zuo M (2018) Synthesis of hierarchical 1D NiO assisted by microwave as anode material for lithium-ion batteries. *Mater Res Bull* 98:155–159
- [40] Shi W, Zhang Y, Key J, Shen P (2018) Three-dimensional graphene sheets with NiO nanobelt outgrowths for enhanced capacity and long term high rate cycling Li-ion battery anode material. *J Power Sources* 379:362–370
- [41] Zhou Z, Chen F, Kuang T, Chang L, Yang J, Fan P, Zhao Z, Zhong M (2018) Lignin-derived hierarchical mesoporous carbon and NiO hybrid nanospheres with exceptional Li-ion battery and pseudocapacitive properties. *Electrochim Acta* 274:288–297
- [42] Li G, Li Y, Chen J, Zhao P, Li D, Dong Y, Zhang L (2017) Synthesis and research of egg shell-yolk NiO/C porous composites as lithium-ion battery anode material. *Electrochim Acta* 245:941–948
- [43] Chamas M, Lippens PE, Jumas JC, Hassounb J, Panero S, Scrosati B (2011) Electrochemical impedance characterization of FeSn₂ electrodes for Li-ion batteries. *Electrochim Acta* 56:6732–6736
- [44] Jiang Y, Zhang D, Li Y, Yuan T, Bahlawane N, Liang C, Sun W, Lu Y, Yan M (2014) Amorphous Fe₂O₃ as a high-capacity, high-rate and long-life anode material for lithium ion batteries. *Nano Energy* 4:23–30
- [45] Tang Y, Zhang Y, Rui X, Qi D, Luo Y, Leow WR, Chen S, Guo J, Wei J, Li W, Deng J, Lai Y, Ma B, Chen X (2016) Conductive inks based on a lithium titanate nanotube gel for

high-rate lithium-ion batteries with customized configuration. *Adv Mater* 28:1567–1576

- [46] Wang X, Hao H, Liu J, Huang T, Yu A (2011) A novel method for preparation of macroporous lithium nickel manganese oxygen as cathode material for lithium ion batteries. *Electrochim Acta* 56:4065–4069

Publisher's Note Springer Nature remains neutral with regard to jurisdictional claims in published maps and institutional affiliations.